



 Cite this: *RSC Adv.*, 2023, 13, 2168

Compositional dependence of Co- and Mo-supported beta zeolite for selective one-step hydrotreatment of methyl palmitate to produce bio jet fuel range hydrocarbons†

 Su-Un Lee,  Tae-Wan Kim, Kwang-Eun Jeong, Sungjune Lee, Min Cheol Shin and Chul-Ung Kim*

For producing a drop-in bio jet fuel, one-step hydrotreatment, which includes deoxygenation, isomerization and cracking in one step, is essential to overcome the typical biofuel drawbacks due to high oxygen content, out of jet fuel range hydrocarbons, and low isomerization degree. Herein, Co- or/and Mo-supported Beta(25) zeolites with various Co/Mo ratios were prepared as transition metal-supported zeolite catalysts without the need for sulfidation of conventional transition metal catalysts. Based on the catalyst characterization, the Co/Mo ratio alters the metal phase with the appearance of CoMoO₄ and the altered Co metal phase strongly influences the acidic properties of Beta(25) by the formation of Lewis (L) acid sites with different strengths as Co₃O₄ and CoMoO₄ for strong and weak L acid sites, respectively. The catalytic activities were investigated for hydrotreatment of methyl palmitate as a biofuel model compound of fatty acid methyl esters. Primarily, Co is required for deoxygenation and Mo suppresses overcracking to enhance the yield of jet fuel range hydrocarbons. The Co/Mo ratio plays an important role to improve the C₈–C₁₆ selectivity by modifying the acidic properties to inhibit excessive cracking. Co₅Mo₁₀/Beta(25) achieved the best catalytic performance with the conversion of 94.2%, C₈–C₁₆ selectivity of 89.7 wt%, and high isomer ratio of 83.8% in organic liquid product. This unique modification of acidic properties will find use in the design of optimal transition metal-supported zeolite catalysts for selective one-step hydrotreatment to produce bio jet fuel range hydrocarbons.

Received 2nd November 2022

Accepted 3rd January 2023

DOI: 10.1039/d2ra06938e

rsc.li/rsc-advances

1. Introduction

The increasing consumption of transportation fuels, the depletion of fossil fuels, and the corresponding environmental concerns have provoked interest in renewable energy sources. By utilizing diverse biomass sources consisting of triglycerides and free fatty acids (FFAs), biomass-derived fuel is a promising candidate to substitute conventional fossil fuels with green biofuel.^{1–3} The common commercialized technology for converting biomass to biofuel is the transesterification of triglycerides or esterification of free fatty acids (FFAs) with methanol, which produces fatty acid methyl esters (FAMES). However, because of the high oxygen content, out of jet fuel range hydrocarbons, and low isomerization degree, FAMES have poor combustion properties such as low heating value, thermal instability, and high freezing point.

The potential of biofuels is highlighted in terms of being able to replace conventional jet fuels with renewable jet fuels, as the world jet fuel demand is likely to grow rapidly by 38% from 2005 to 2025.⁴ Ultimately, feasible alternatives for conventional jet fuel is a ‘drop-in’ jet fuel that is completely compatible with conventional jet fuel and existing engines in the absence of a requirement for any modifications. However, it is difficult to replace conventional jet fuels with unrefined biofuels and satisfy stringent international requirements, such as excellent oxidative stability, freezing points below –40 °C, and heat of combustion greater than 42.8 MJ kg^{–1}.⁵ To achieve a ‘drop-in’ jet fuel from biofuel, one-step hydrotreatment is essential to overcome the typical biofuel disadvantages, caused by higher oxygen content and out of jet fuel range hydrocarbons, and low isomerization degree. In general, the first step is deoxygenation (DO) to produce *n*-alkanes, and the following step is the cracking and isomerization of *n*-alkanes to produce iso-alkanes in the jet fuel range from C₈ to C₁₆. The integration of DO, isomerization and cracking in one step can raise the industrial applicability with economic gains, but the development of ideal catalysts is still far behind industrial requirements.⁶

Chemical & Process Technology Division, Korea Research Institute of Chemical Technology, 141, Gajeong-ro, Yuseong-gu, Daejeon 34114, South Korea. E-mail: cukim@kriict.re.kr; Fax: +82-42-860-7590; Tel: +82-42-860-7504

† Electronic supplementary information (ESI) available. See DOI: <https://doi.org/10.1039/d2ra06938e>



To upgrade the quality of bio jet fuel, various metal-supported metal oxide and zeolite catalysts have been investigated, such as Rh/ZrO₂,⁷ CoMo/Al₂O₃,⁸ Mo/ZSM-5,¹ Ni/Beta,^{9,10} and so forth. The use of metal oxide as a support can stabilize the active metal catalysts with high dispersion for high activity and stability such as mesoporous support¹¹ and LDH-derived metal catalysts.^{12,13} More than that, zeolites are expected to outperform the intrinsic catalytic performance of metal catalysts because they provide a porous structure to reduce the diffusion limitation⁹ and acid sites for acid-catalyzed reactions^{14,15} and isomerization to change *n*-alkanes to iso-alkanes.¹⁵ These studies have found that a high-performance zeolite catalyst can be achieved by optimizing the porosity, acidity, and composition. Meanwhile, among the conventional metal catalysts for DO, noble metal catalysts, such as Rh and Pt, exhibit high efficiency, but their exorbitant costs restrict large-scale application. In the case of conventional transition metal catalysts, such as CoMo or NiMo, the introduction of sulfur for transition metal sulfides is necessary to achieve activity comparable to that of noble metal catalysts, which cause the serious deactivation and product contamination by sulfur leaching.^{8,16} Combining the advantages of zeolites and transition metals as bi-functional catalysts, transition metal-supported zeolite catalysts are highly attractive to cover the low activity of transition metal without sulfidation by exploiting the catalytic properties of zeolites. However, only a few reports have dealt with nonsulfided CoMo or NiMo-supported zeolite catalysts.¹⁷

In this work, we prepared Co- or/and Mo-supported Beta(25) zeolites to investigate the effects of transition metal-supported zeolite catalysts on the catalytic properties for selective one-step hydrotreatment of methyl palmitate as a model compound of FAMES in order to produce a drop-in bio jet fuel. As representative examples of the second and third generation of renewable biofuels that do not compete with food crops such as the first generation biofuels, the biofuels derived from such as styra japonicas and microalgae contain methyl palmitate and unsaturated fatty acids in double bonds. In the meantime, unsaturated materials in double bonds can be not only easily saturated by hydrogenation before subsequent hydrotreatment,¹⁸ but also upgraded for biochemicals through metathesis.¹⁹ Therefore, methyl palmitate was selected as model compound of FAMES to investigate selective one-step hydro-treatment. Beta zeolite was chosen because large pore radius and high surface area can provide the diffusion of large molecules of FAMES and generate small hydrocarbon molecules in the bio-jet fuel range.^{20,21} According to the change in the composition ratio of Co and Mo, the metal phase was varied with not only each single metal oxides but also CoMoO₄ as the third metal phase. Compared with single metal-supported beta zeolite catalysts, the Co- and Mo-supported Beta(25) zeolites enabled a unique modification of acidic properties with CoMoO₄ and the optimal condition enhanced the catalytic properties including high methyl palmitate conversion and selective C₈–C₁₆ range alkanes with high isomer ratio as desired products for jet fuel range hydrocarbons. This work provides a meaningful reference for Co- and Mo-supported beta zeolite

catalysts for selective one-step hydrotreatment of bio jet fuel range hydrocarbons.

2. Experimental section

2.1 Catalyst preparation

2.1.1 Synthesis of Co- or/and Mo-supported Beta(25) zeolites. The Co- or/and Mo-supported Beta(25) zeolites were prepared by a conventional wet-impregnation method. In the first step, commercial Beta(25) zeolite (SiO₂/Al₂O₃ molar ratio of 25, Zeolyst international) was calcined at 550 °C for 5 h in an air atmosphere, which converted from the NH₃-form to the H⁺-form. The obtained Beta(25) zeolite was dissolved in distilled water and stirred for 1 h. Simultaneously, an aqueous solution of an appropriate concentration of Co(NO₃)₂·6H₂O (98%, Sigma-Aldrich) or/and (NH₄)₆Mo₇O₂₄·4H₂O (≥99.0%, Sigma-Aldrich) was prepared with being stirred for 1 h. Then, the mixed aqueous solution of metal precursors was added into the Beta(25) zeolites in the distilled water and vigorously stirred for 12 h. The wet-impregnated catalyst was collected by evaporating water solvent under vacuum, dried at 100 °C for 3 h, and calcined at 550 °C for 5 h in an air atmosphere. As bimetallic catalysts, the Co- and Mo-supported Beta(25) zeolites were denoted as “Co_xMo_y/Beta(25)” including Co₁₀Mo₅/Beta(25), Co₁₀Mo₁₀/Beta(25), Co₅Mo₁₀/Beta(25), Co₃Mo₁₀/Beta(25), and Co₂Mo₁₀/Beta(25), where ‘x’ and ‘y’ are the weight % of Co and Mo, respectively. As monometallic catalysts, Co₁₀/Beta(25) and Mo₁₀/Beta(25) containing metal weight loading of 10 weight% were prepared following an identical experimental procedure except that an aqueous solution of one metal precursor with the corresponding metal content were used.

2.2 Catalyst characterization

The characterizations of the catalysts were performed using XRD, Raman, XPS, TEM, H₂-TPR, N₂ sorption, NH₃-TPD, and FTIR analysis.

X-ray diffraction (XRD) patterns were obtained using a Rigaku Ultima IV Diffractometer operating at 40 kV and 40 mA with Cu-Kα radiation.

Raman spectra were measured with Nanophoton RAMANforce Raman spectrometer using 532 nm laser excitation.

X-ray photoelectron spectroscopy (XPS) spectra were obtained using a KRATOS AXIS NOVA spectrometer with monochromatic Al Kα X-ray (1486.6 eV). All the XPS data was calibrated based on C 1s peak at 284.8 eV.

Transmission electron microscopy (TEM) images, high-angle annular dark field scanning transmission electron microscopy (HAADF-STEM) and energy-disperse X-ray spectrometry (EDS) mapping images were obtained by a field emission gun transmission and scanning transmission electron microscope (FEG-S/TEM, FEI-Talos F200S) operating at 200 kV.

Hydrogen-temperature programming reduction (H₂-TPR) was estimated by BELCAT-B equipped with a thermal conductivity detector (TCD). The sample of 0.05 g was packed in a U-tube quartz cell with quartz wool. As a pretreatment step, the sample was treated in a He flow by heating to 200 °C at 10 °

C min⁻¹ and stabilized for 1 h. After cooling down to 40 °C, He flow was changed to a H₂ (3.5%)/Ar flow and maintained for 3 h. When the TCD signal was stabilized, the sample was heated to 1000 °C at 10 °C min⁻¹ in a H₂ (3.5%)/Ar flow, and TCD signals were recorded by the temperature. The water product was trapped by passing the effluent gas from the reactor through a trap of molecular sieves 13X.

Nitrogen (N₂) adsorption-desorption experiments were carried out by a Micrometrics TriStar 3000 instrument. The sample was reduced in a tubular furnace by H₂ flow at 500 °C for 4 h for the same pretreatment with the catalytic reaction test. Then, the reduced sample was degassed under vacuum condition at 300 °C for 5 h and N₂ adsorption-desorption experiment was conducted at -196 °C. Total surface area and pore volume were calculated by the BET equation and the N₂ adsorption method, respectively. Surface area and pore volume of micro-pore and mesopore were estimated by *t*-plot method.

The temperature programming desorption of ammonia (NH₃-TPD) was measured by BELCAT-B equipped with a TCD. The sample was reduced in a tubular furnace by H₂ flow at 500 °C for 4 h for the same pretreatment with the catalytic reaction test. Then, the sample of 0.05 g was packed in a U-tube quartz cell with quartz wool and pretreated at 150 °C for 2 h to remove the moisture. The sample was placed in a NH₃ (30 mol%)/He flow for 30 min, and weakly physisorbed ammonia was eliminated by purging in the He flow for 90 min. The sample was heated from 100 °C to 700 °C at 10 °C min⁻¹ in the He flow, and the amount of the desorbed ammonia was recorded by TCD signals.

For Fourier transformation infrared (FTIR) spectra of adsorbed pyridine, the sample was prepared after the reduction in a tubular furnace by H₂ flow at 500 °C for 4 h for the same pretreatment with the catalytic reaction test. Then, thin wafer (*ca.* 13 mg) was produced by pressing the sample in the type of powder and pretreated in an IR cell at 150 °C for 2 h to remove the moisture. After cooling down to 60 °C, pyridine was purged to adsorb on the acidic sites of pretreated samples at 60 °C for 10 min. The physisorbed and weakly bound species were removed under a He flow at 150 °C for 3 h. IR spectrum was obtained from an FT-IR spectrometer (Thermo SCIENTIFIC Nicolet6700) equipped with thermal detector.

2.3 Catalytic performance tests

The catalytic reaction tests of methyl palmitate as a biofuel model component of fatty acid methyl esters were carried out in a semi-batch reaction system at 280 °C under a pressure of 20 bar for 2 h (the catalytic conversions of palmitic acid and hexadecane were also followed the same procedures). Before conducting the catalytic performance, the catalyst was reduced in a tubular furnace by H₂/N₂ mixed flow at 500 °C for 4 h. Then, 1.0 g of the catalyst and 10 g of methyl palmitate in the absent of solvent were loaded in the reactor (100 ml, Parr Instrument Co.). Prior to the reaction, the atmosphere in the reactor was charged with purging nitrogen and then hydrogen was pressurized at 20 bar. The temperature in the reactor was raised up to 280 °C and held for 2 h. The reaction was initiated by adjusting the

atmosphere to 20 bar of hydrogen and proceeded with stirring (500 rpm). After 2 h, the reaction was terminated by rapidly cooling down to room temperature. The liquid and solid products were separated by centrifugation after the reaction.

The liquid product was measured on a balance for mass balance by weight change of before and after the reaction. Prior to gas chromatographic analysis, the liquid samples had to be dissolved in pyridine and silylated with *N,O*-bis(trimethyl)-trifluoroacetamide (BSTFA) including eicosane as an internal standard for the quantitative analysis. The silylation treatment is required to prevent clogging of the GC column due to the reaction between organic acids and GC packing materials because the product can be produced not only as hydrocarbon component but also as free fatty acid, which is an acid component. Then, the silylated samples were analyzed with a gas chromatograph (YoungLin GC 3000) equipped with HP-5 column and flame ionization detector (FID).

$$\text{Conversion of methyl palmitate} = \left(\frac{\text{moles of converted methyl palmitate}}{\text{moles of the starting methyl palmitate}} \right) \times 100\%$$

$$\text{Selectivity of products in organic liquid product} = \left(\frac{\text{moles of each product}}{\text{moles of total products}} \right) \times 100\%$$

3. Results and discussion

3.1 Compositional characterization of catalysts

The catalysts in the oxidized form were obtained by wet-impregnation and subsequent calcination. As bimetallic catalysts, the Co- and Mo-supported Beta(25) zeolites were described as “Co_{*x*}Mo_{*y*}/Beta(25)” including Co₁₀Mo₅/Beta(25), Co₁₀Mo₁₀/Beta(25), Co₅Mo₁₀/Beta(25), Co₃Mo₁₀/Beta(25), and Co₂Mo₁₀/Beta(25), where ‘*x*’ and ‘*y*’ are the weight% of Co and Mo, respectively. As monometallic catalysts, Co₁₀/Beta(25) and Mo₁₀/Beta(25) were prepared containing 10 weight% of Co and Mo, respectively. The crystalline phases were revealed by the X-ray powder (XRD) patterns as shown in Fig. 1. The XRD pattern of Co₁₀/Beta(25) demonstrates the characteristic diffraction peaks of Co₃O₄ at 19.1°, 31.4°, 36.9°, 44.7°, 55.8°, 59.5°, and 65.4°, which are assigned to (111), (220), (311), (400), (422), (511), (440) planes, respectively. On the other hands, the crystalline phase of Mo species is not observed in the XRD pattern of Mo₁₀/Beta(25), so it can be attributed to amorphous phase and/or high dispersion below the size of the XRD detection limit. When Co and Mo were co-impregnated in the Co- and Mo-supported Beta(25), a new diffraction peak was detected at 2θ of 26.4° corresponding to the (002) plane of CoMoO₄. It means that co-impregnation of Co and Mo induces the formation of CoMoO₄ phase. When the content of Co was decreased below Co₃Mo₁₀/Beta(25) and Co₂Mo₁₀/Beta(25), the diffraction peaks of Co₃O₄ disappeared; therefore, it is assumed that Co would form CoMoO₄ with Mo rather than Co₃O₄ until the unconverted Co to CoMoO₄ remains in excess of Mo.²² To confirm the Mo effect on the dispersion of Co species,^{23,24} the mean crystallite size of Co₃O₄ was calculated from the diffraction peak at 2θ = 36.9° with the Scherrer equation; 18.2 nm for Co₁₀/Beta(25),

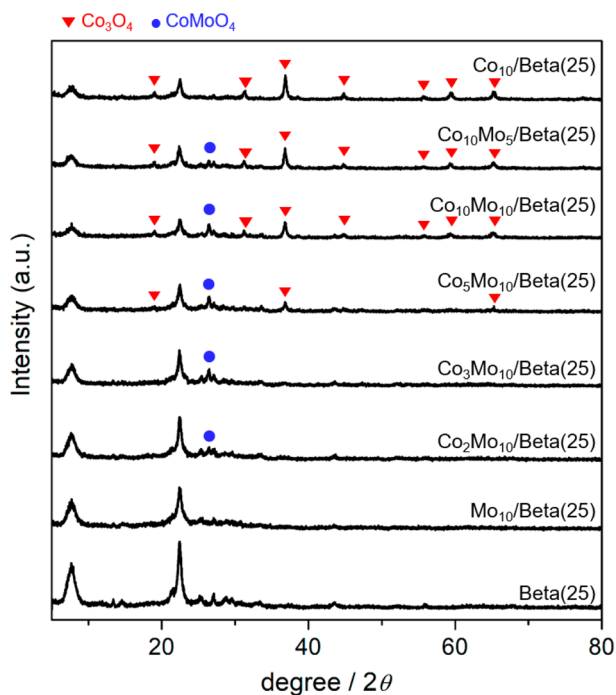


Fig. 1 XRD patterns of Co- or/and Mo-supported Beta(25) and Beta(25) obtained by wet-impregnation and subsequent calcination. The positions of characteristic peaks are referenced from the JCPDS database (BEA: PDF# 01-074-8795, Co_3O_4 : PDF# 00-042-1467, CoMoO_4 : PDF# 00-021-0868).

18.4 nm for $\text{Co}_{10}\text{Mo}_5/\text{Beta}(25)$, 15.7 nm for $\text{Co}_{10}\text{Mo}_{10}/\text{Beta}(25)$, and 16.6 nm for $\text{Co}_5\text{Mo}_{10}/\text{Beta}(25)$. The mean crystallite size of Co_3O_4 seems to decrease from around 18 nm to around 16 nm for sample loaded with more than 10 wt% Mo, but within the range of no significant difference. Regarding the crystallinity of Beta zeolite, two prominent peaks appear at 2θ of 7.6° and 22.6° indexed to the (101) and (302) planes of Beta zeolite. However, the peak intensities of Beta zeolite weaken with metal loading, especially Co, indicating the incorporation of metal species with zeolite framework,²⁵ and it will be considered with H_2 -TPR results.

To further clarify the phases of supported metal oxide on the Beta(25) zeolites, Raman spectra were obtained, as shown in Fig. 2. $\text{Co}_{10}/\text{Beta}(25)$ shows peaks at 474, 515, 615, and 681 cm^{-1} in the range of $400\text{--}800\text{ cm}^{-1}$, which correspond to the typical E_g , F_{2g}^2 , F_{3g}^3 , and A_{1g} vibration modes of crystalline Co_3O_4 ,²⁶ respectively. $\text{Mo}_{10}/\text{Beta}(25)$ shows peaks at 952 and 907 cm^{-1} , which are attributed to the symmetric stretching of the $\text{Mo}=\text{O}$ bond in the polymeric molybdate species.²⁷ The intense peak at 952 cm^{-1} is considered to be octahedral molybdate species interacting weakly with the support,^{28–30} and the weak peak at 907 cm^{-1} originates from isolated tetrahedral molybdates species interacting strongly with the support.³¹ Generally, bulk MoO_3 crystallites display the Raman peaks around 990 cm^{-1} , 820 cm^{-1} , and 300 cm^{-1} corresponding to the bending mode of $\text{M}=\text{O}$ bonds, the stretching mode of $\text{M}=\text{O}$, and the antisymmetric stretching mode of $\text{Mo}-\text{O}-\text{Mo}$, respectively.³² In our case, the absence of Raman peaks from bulk MoO_3 crystallites

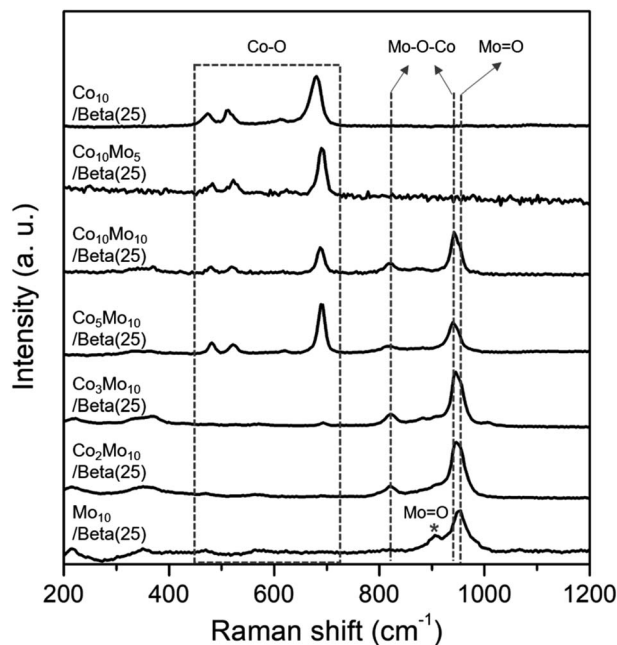


Fig. 2 Raman spectra of Co- or/and Mo-supported Beta(25) zeolites after the wet-impregnation and subsequent calcination.

suggests the small size of $(\text{MoO}_3)_n$ oligomers, which can also explain the absence of X-ray diffraction for MoO_3 .³³ As for Co- and Mo-supported Beta(25), Raman spectra confirm the formation of CoMoO_4 with the appearance of new peak at 941 cm^{-1} and 820 cm^{-1} , which are assigned to the $\text{Mo}-\text{O}-\text{Co}$ stretching vibrations of CoMoO_4 .³⁴ However, the Raman peaks for crystallite Co_3O_4 are not detected in $\text{Co}_2\text{Mo}_{10}/\text{Beta}(25)$ and $\text{Co}_3\text{Mo}_{10}/\text{Beta}(25)$ with low Co/Mo ratio, and start to appear from $\text{Co}_5\text{Mo}_{10}/\text{Beta}(25)$. In consistent with the XRD results, it supports the preference for the formation of CoMoO_4 than mono metal oxides, and thus Co_3O_4 is concurrently formed with CoMoO_4 above a certain Co/Mo ratio, such as from $\text{Co}_5\text{Mo}_{10}/\text{Beta}(25)$, in these findings. The difference in metal phase could be beneficial for better understanding the effect of the Co/Mo ratio on the following physicochemical and catalytic properties.

The XPS experiments were conducted in the binding energy (BE) ranges of corresponding to Co 2p and Mo 3d to elucidate the types of surface metal species in the prepared catalysts as shown in Fig. S1†. The Co 2p XPS spectrum of $\text{Co}_{10}/\text{Beta}(25)$ (Fig. S1a†) presents intense doublet peaks at 797.3 eV (Co $2p_{1/2}$) and 781.2 eV (Co $2p_{3/2}$), and a satellite accompanying each doublet at higher BEs. Considering that $\text{Co}_{10}/\text{Beta}(25)$ contains Co_3O_4 according to the XRD analysis, it has relatively higher BE than the typical BE of Co_3O_4 observed at 779.9 eV (Co $2p_{3/2}$)³⁵ by 1.3 eV. Similarly, the Mo 3d XPS spectrum of $\text{Mo}_{10}/\text{Beta}(25)$ in Fig. S1c† exhibits the BE of Mo $3d_{5/2}$ at 233.5 eV , and it is also higher than the typical BE for Mo^{6+} (232.8 eV)³⁶ by 0.7 eV. The upward shift in the BEs of Co and Mo are caused by the deficient electron density of the wet-impregnated metal species in Beta(25). It was previously reported that Brønsted acid sites of zeolites act as electron acceptors and induce the electron transfer from metal particles to zeolites.^{37,38} Therefore, it is

worth mentioning that metal–support interaction, especially on Brønsted acid sites. On the other hand, the Co 2p XPS of $\text{Co}_5\text{Mo}_{10}/\text{Beta}(25)$ in Fig. S1b[†] presents the peak of Co 2p_{3/2} at 783.0 eV, which is attributed to Co³⁺ in the form of CoMoO_4 the typical BE of CoMoO_4 observed at 781.2 eV³⁹ with shift to higher BE by 1.8 eV. With regard to the Mo 3d XPS of $\text{Co}_5\text{Mo}_{10}/\text{Beta}(25)$ in Fig. S1d,[†] it can be deconvoluted into two peaks, which can be indexed to Mo⁶⁺ at 233.6 eV and CoMoO_4 at 232.3 eV. The result confirms the existence of not only CoMoO_4 but also MoO_3 , which cannot be revealed from the XRD analysis. Therefore, the existence of MoO_3 cannot be excluded even in the Co- and Mo-supported Beta(25) zeolites with low Co/Mo ratio in spite of that the preference of formation of CoMoO_4 .

The spatial distribution of elemental composition in association with each metal phase was observed by transmission electron microscopy (TEM), high-angle annular dark-field scanning TEM (HAADF-STEM), and the corresponding energy-dispersive X-ray spectroscopy (EDS) elemental mapping images as shown in Fig. 3. As for $\text{Co}_{10}/\text{Beta}(25)$, the Co_3O_4 phase was confirmed as an agglomerated Co domain independent of Beta(25) zeolites by TEM image in Fig. 3a with the dark contrast and the corresponding HAADF-STEM-EDS mapping image in Fig. 3d with the green color. In the case of $\text{Mo}_{10}/\text{Beta}(25)$, the Mo domain is not distinctly marked with different contrast in the TEM image (Fig. 3b), and the compositional distribution of Mo shows good matching with those of Si and Al in the HAADF-STEM-EDX mapping image (Fig. 3e) due to high dispersion over Beta(25) zeolite. When Co and Mo are co-impregnated in $\text{Co}_5\text{Mo}_{10}/\text{Beta}(25)$, the Mo species are observed with an overlap of the Co domain as shown in Fig. 3f, which is also represented by the dark contrast in the TEM image in Fig. 3c. This region

simultaneously observed with Co and Mo has the CoMoO_4 phase. In contrast, a non-overlapping Co domain with Mo has the additional Co_3O_4 .

By analyzing H₂-temperature-programmed reduction (TPR) in Fig. 4, the transformation of metal oxide phases was

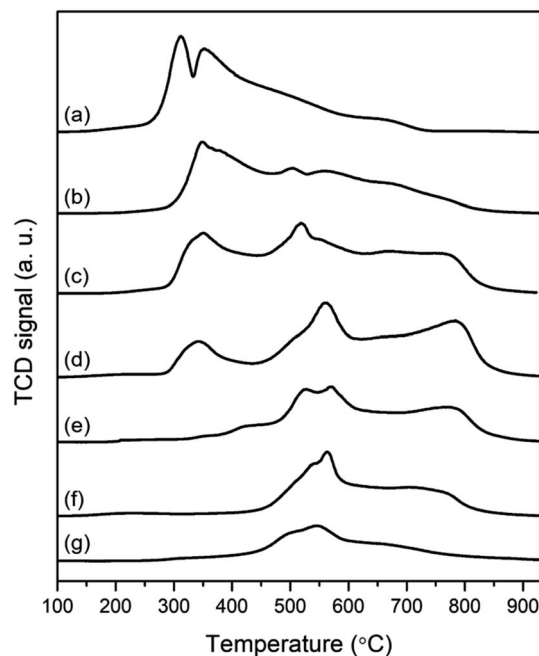


Fig. 4 H₂-TPR of the catalysts after the wet-impregnation and subsequent calcination; (a) $\text{Co}_{10}/\text{Beta}(25)$, (b) $\text{Co}_{10}\text{Mo}_5/\text{Beta}(25)$, (c) $\text{Co}_{10}\text{Mo}_{10}/\text{Beta}(25)$, (d) $\text{Co}_5\text{Mo}_{10}/\text{Beta}(25)$, (e) $\text{Co}_3\text{Mo}_{10}/\text{Beta}(25)$, (f) $\text{Co}_2\text{Mo}_{10}/\text{Beta}(25)$, and (g) $\text{Mo}_{10}/\text{Beta}(25)$.

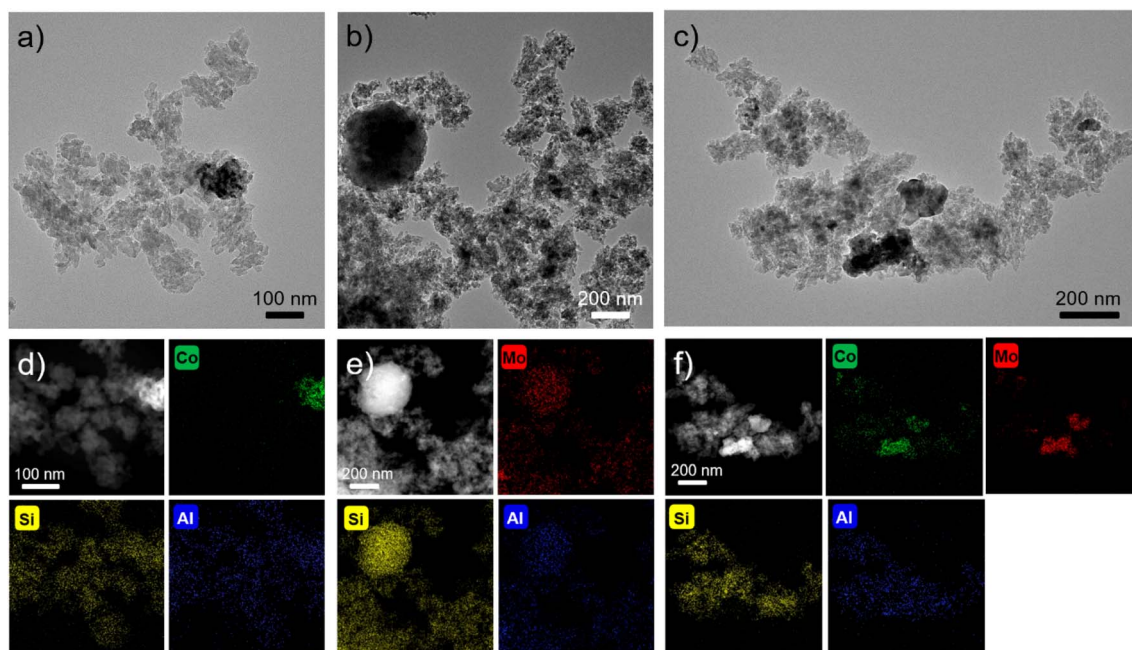


Fig. 3 TEM (a–c) and corresponding HADDF-STEM-EDX-mapping (d–f) images of (a and d) $\text{Co}_{10}/\text{Beta}(25)$, (b and e) $\text{Mo}_{10}/\text{Beta}(25)$, and (c and f) $\text{Co}_5\text{Mo}_{10}/\text{Beta}(25)$ after the wet-impregnation and subsequent calcination.

estimated according to reduction temperature. As shown in Fig. 4, Co₁₀/Beta(25) exhibits two intense peaks at 313 °C and 354 °C, which can be attributed to the reduction of Co₃O₄ through Co³⁺ to Co²⁺ and Co²⁺ to Co⁰, respectively.⁴⁰ In the case of Mo₁₀/Beta(25), the H₂-TPR profile has two overlapped peaks at 492 °C and 548 °C, and a broad peak over 589 °C. The consecutive reductions are attributed to MoO₃ (Mo⁶⁺) to MoO₂ (Mo⁴⁺) and then to Mo (Mo⁰). Considering that the H₂-TPR profiles of Co₁₀/Beta(25) and Mo₁₀/Beta(25) show the overlapped and broad peaks, it is possible that the wet-impregnated metal species loaded on the surface of zeolites establish different degree of metal-support interaction and thus reduced at different temperature. From the H₂-TPR profile of the Co and Mo-supported Beta(25) zeolites, the reduction of Co₃O₄ was detected as the first peak in the temperature range of 285 °C and 450 °C. As decreasing the Co:Mo ratio, the intensity and temperature range of the first peak gradually decreased, which indicates that less Co₃O₄ was formed with improved reducibility. As the XRD results confirmed that the crystallinity of Beta zeolite was better maintained with low Co content, the improved reducibility at the low Co:Mo ratio compared to Co₁₀/Beta(25) could be attributed to the weak interaction between metal and zeolite framework. Then, H₂-consumption from the reduction of Co₃O₄ was finally disappeared in Co₂Mo₁₀/Beta(25) and Co₃Mo₁₀/Beta(25). It is in good agreement with that Co combines with Mo to form CoMoO₄ rather than independently becoming cobalt oxides when Co and Mo are co-impregnated.²² Instead, the reduction of CoMoO₄ phase was observed with new three reduction peaks at higher temperature than that of cobalt oxides. More in detail, the first two peaks between 450–610 °C are attributed to the reduction of CoMoO₄ through CoMoO₄ to CoMoO₃ and CoMoO₃ to Co₃Mo, respectively. The latter at approximately 780 °C is assigned to a further reduction of Co₃Mo to Co₂Mo₃.⁴¹ Especially, the reduction of CoMoO₄ to Co₃Mo accompanies the additional formation of MoO₃ and Mo₄O₁₁,⁴² so there is a limitation of separating the reduction from MoO₃ due to overlapping H₂-consumption. Before conducting catalytic reaction test for hydrotreatment of methyl palmitate at 280 °C under a hydrogen pressure of 20 bar, the catalysts were pretreated under hydrogen atmosphere at 500 °C. From the XRD pattern in Fig. S2,[†] the phase transformation of metal oxides after hydrogen reduction was identified to define the active phase. The XRD pattern of the reduced Co₁₀/Beta(25) confirms the co-existence of CoO and metallic Co, because the complete reduction of cobalt oxides to metallic cobalt requires to be reduced up to 740 °C according to the TPR analysis. The reduced Co and Mo-supported Beta(25) displayed the typical XRD peaks of Co and Co₃Mo except CoO. As the Co:Mo ratio decreases, the peak intensity for Co₃Mo increases and that for monometallic Co decreases. Thus, it also demonstrates that the reduced Co and Mo-supported Beta(25) favors to obtain bimetallic Co and Mo oxides/metal rather than single Co metal/oxide because all the Co species would form CoMoO₄ with Mo and the excess Co form Co₃O₄. Therefore, it concludes that all the Co- and Mo-supported Beta(25) contains CoMo alloy metal/oxide and Mo oxides after hydrogen reduction, but the presence of Co metal/oxides are dependent on the Co/Mo ratio. Combined

with the above analysis results, the control of the Co/Mo ratio does not simply change the loading amount of each metals/oxides, but diversifies the phase of a single metal/oxide into a mixed metal/oxide with the appearance of CoMoO₄ phase. Therefore, it is meaningful to focus on the phase difference in relation with noticeable change in their catalytic properties.

3.2 Modified properties by the Co/Mo ratio with respect to catalytic property: surface area, pore structure and acidity

Typically, the main factors that affect the catalytic activity of a catalyst are surface area, pore structure and acidic property. Among them, surface area and pore volume are basic factors that provide reaction sites and promote diffusion of reactants and products, and thus estimated from the isothermal adsorption and desorption isotherms of N₂ at 77 K (Table S1[†]) with the BET and *t*-plot method. The catalysts obtained by the wet-impregnation and subsequent calcination were reduced following the same pretreatment conditions of the catalytic reaction test to reflect the same state in the catalytic reaction test. Compared to the pristine Beta(25) zeolite, the surface area and pore volume of the Co- or/and Mo-supported Beta(25) zeolites were reduced, but the difference according to the amount of metal loading was insignificant. Thus, the effects of the surface area and pore volume were excluded to find the factors determining the difference in catalytic activity of individual Co- or/and Mo-supported Beta(25) zeolites.

For the analysis of the acidic property, an NH₃-temperature-programmed desorption (TPD) was measured in Fig. 5 and the amount of acid sites was estimated in Table 1. Note that all the samples were also reduced prior to NH₃-TPD analysis, which is the same pretreatment used for the catalytic reaction test. The supported metal catalyst does not appear to be relevant with respect to the total amount of acid sites. In order to further clarify the difference in acidic properties according to the metal phase difference, the Co- or/and Mo-supported Beta(25) zeolites were classified into four categories based on the catalysts obtained by the wet-impregnation and subsequent calcination for clarity: group I: Co₁₀/Beta(25) with Co₃O₄; group II: Co₁₀Mo₅/Beta(25), Co₁₀Mo₁₀/Beta(25), and Co₅Mo₁₀/Beta(25) with Co₃O₄ and CoMoO₄ + MoO₃; group III: Co₃Mo₁₀/Beta(25) and Co₂Mo₁₀/Beta(25) with CoMoO₄ and MoO₃; group IV: Mo₁₀/Beta(25) with MoO₃ as described in Table 1. With respect to the NH₃-TPD of the pristine Beta(25) zeolite in Fig. 5a, the NH₃ desorption peaks are deconvoluted into three desorption peaks centered in the temperature ranges of 100–200 °C (weak acidity), 200–350 °C (medium acidity), and above 350 °C (strong acidity) using the Gaussian curve fitting method. The detailed deconvolution results are demonstrated in Fig. S3,[†] and the corresponding peak temperature and density of acid sites are calculated in Table 1. As shown, the NH₃-TPD of Beta(25) indicates weak and medium acidity in the main acid sites, but also show a very small amount of strong acidity. When Co is added to Beta(25) zeolite for Co₁₀/Beta(25) of group I, the amounts of weak and medium acid sites decrease and a new intensive desorption peak appears at 371 °C. A similar phenomenon has been reported in the literature, and these results were attributed to the

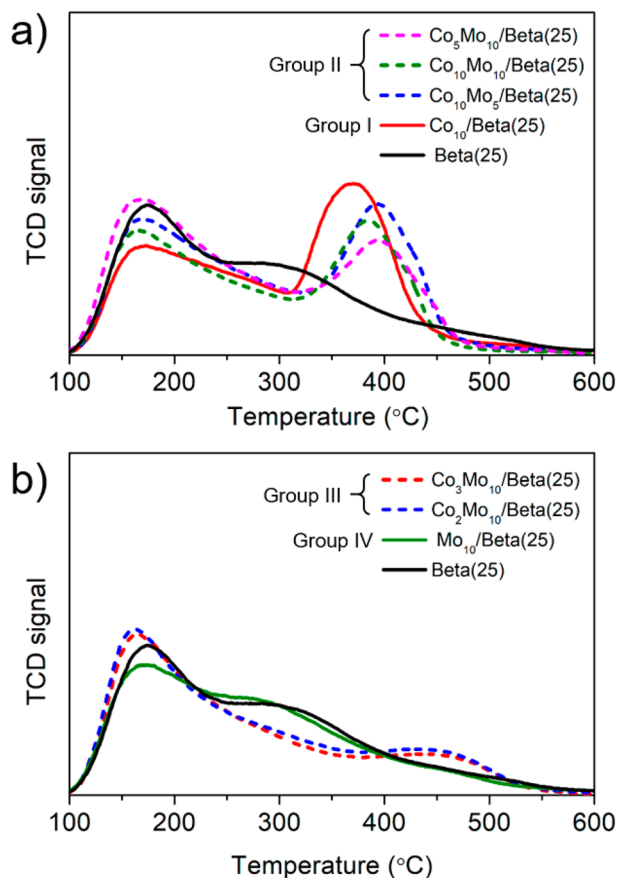


Fig. 5 NH_3 -TPD of catalysts after the reduction under the same pretreatment condition of the catalytic reaction test: (a) $\text{Co}_{10}/\text{Beta}(25)$, $\text{Co}_{10}\text{Mo}_5/\text{Beta}(25)$, $\text{Co}_{10}\text{Mo}_{10}/\text{Beta}(25)$, $\text{Co}_5\text{Mo}_{10}/\text{Beta}(25)$, and $\text{Beta}(25)$, and (b) $\text{Mo}_{10}/\text{Beta}(25)$, $\text{Co}_2\text{Mo}_{10}/\text{Beta}(25)$, $\text{Co}_3\text{Mo}_{10}/\text{Beta}(25)$, and $\text{Beta}(25)$, which are separately classified according to the combination of metal phases.

fact that the weak acid sites on the surface of hydroxyl groups are covered by Co species and the strong acid sites are created by the tendency of Co to form a tetrahedral CoO_4^{2-} arrangement in the zeolite framework.^{43–45} On the other hand, the addition of Mo induces a slight decrease in the NH_3 -desorption peak intensity at low temperature and a peak shift of the three NH_3 -desorption peaks to the lower temperature range in the NH_3 -TPD when compared with $\text{Beta}(25)$ and $\text{Mo}_{10}/\text{Beta}(25)$ in Fig. 5b and Table 1. In the case of the Co- and Mo-supported $\text{Beta}(25)$ zeolites belonging to group II and III, the NH_3 -desorption peak generally decreased at weak and medium temperature, and the peak appeared at high temperature showed a tendency to increase, which was consistent with $\text{Co}_{10}/\text{Beta}(25)$. As decreasing the Co/Mo ratio from $\text{Co}_{10}\text{Mo}_5/\text{Beta}(25)$ to $\text{Co}_2\text{Mo}_{10}/\text{Beta}(25)$, the intensity of NH_3 -desorption peak shift from high temperature to low temperature while maintaining a similar total amount (see also Table 1). Noticeably, group III showed a dramatic decrease in the NH_3 -desorption peak at high temperature and the position of the peak also appeared at higher temperature range of 410–430 °C, unlike 380–400 °C in group II. In terms of Co metal phase, group II contains Co_3O_4 in

the same forms as group I and CoMoO_4 , but group III contains Co only as CoMoO_4 . Therefore, it can be seen that the Co loading induces different effects on the acidic properties in relation to the metal phase in which Co is present.

To further clarify the types of the acid sites in the catalysts between Brønsted (B) and Lewis (L) acid site, the Fourier transformation infrared (FTIR) spectra of adsorbed pyridine were obtained as shown in Fig. S4.† The quantity of B and L acid sites are reflected on the IR peaks of 1550 cm^{-1} and 1450 cm^{-1} , respectively, as the stretching bands of pyridine adsorbed to each acid site. As described in Table 1, the B/L ratio was calculated from the ratio of the corresponding peak area, and each quantity is determined by multiplying the B/L ratio from the FTIR spectra of adsorbed pyridine and the total acid site concentration from the NH_3 -TPD profiles. Relative to $\text{Beta}(25)$, $\text{Co}_{10}/\text{Beta}(25)$ exhibits a significant decrease in the B/L ratio from 0.88 to 0.15 due to the formation of L acid sites. In general, the supported Co component can act as an acceptor of electron pairs as L acid sites.^{43,46} Along with the NH_3 -TPD results showing strong acid sites formation on the Co-supported $\text{Beta}(25)$ zeolites, new strong acid sites can be interpreted as L acid sites. Meanwhile, $\text{Mo}_{10}/\text{Beta}(25)$ causes the large increase in the B/L ratio from 0.88 to 1.03, and the quantities of each type of acid site demonstrate the formation of B acid sites and the disappearance of L acid sites. Regarding new B acid sites in the Mo-supported $\text{Beta}(25)$ zeolites, a likely cause is the tetrahedral Mo species strongly bound in a monodentate manner to Al in the support or Mo in a polymolybdate layer, according to Rajagopal *et al.*, who made a similar observation over $\text{MoO}_3/\text{silica-aluminas}$.^{47,48} The coordination of Mo as tetrahedral molybdates over $\text{Beta}(25)$ in $\text{Mo}_{10}/\text{Beta}(25)$ was confirmed by the Raman spectra shown in Fig. 2. Since the NH_3 -TPD of $\text{Mo}_{10}/\text{Beta}(25)$ showed the reduced peak intensity at low temperature and the peak shift to lower temperature, the acid strength of the increased B and decreased L acid sites should result in the decreased acidity than $\text{Beta}(25)$. Combined with the characterization of the NH_3 -TPD and FTIR spectra of adsorbed pyridine, Co results in the formation of strong L acid sites, and Mo generates weak B acid sites in the single metal-supported $\text{Beta}(25)$. When Co and Mo were co-supported over the $\text{Beta}(25)$ zeolites, the quantity of L acid sites increased by increasing the Co/Mo ratio as observed on the $\text{Co}_{10}/\text{Beta}(25)$. However, unlike the $\text{Mo}_{10}/\text{Beta}(25)$, B acid sites decreased over the Co- and Mo-supported $\text{Beta}(25)$ zeolites. As previously reported by Kiviat *et al.*, Co–Mo/ Al_2O_3 showed fewer B acid sites than Mo/ Al_2O_3 due to the Co ions interacting with the molybdate (Mo^{6+}) phase.⁴⁹ More importantly, group III showed a large increase in the formation of L acid sites similar to $\text{Co}_{10}/\text{Beta}(25)$ from FTIR spectra of adsorbed pyridine, but a slight increase in the amount of strong acid sites the from the NH_3 -TPD profiles. Therefore, the introduction of Co causes the formation of L acid sites with different strengths, such as strong L acid sites for Co_3O_4 and weak L acid sites for CoMoO_4 depending on Co metal phase. From the above characterization, it was found that each metal species had different modifying effect on the acidic properties depending on single metal or bimetallic phase.

Table 1 Acidic properties estimated from NH₃-TPD profiles and FTIR spectra of adsorbed pyridine for each group classified separately according to the combination of metal phases. The catalysts were reduced under the same pretreatment condition of the catalytic reaction test

Group	Sample	Metal phase	NH ₃ -TPD						FTIR of adsorbed pyridine				
			Weak acid sites ^a		Medium acid sites ^a		Strong acid sites ^a		Total acid sites		B ^b (mmol g ⁻¹)	L ^b (mmol g ⁻¹)	B/L ^b
			T (°C)	Density (mmol g ⁻¹)	T (°C)	Density (mmol g ⁻¹)	T (°C)	Density (mmol g ⁻¹)	T (°C)	Density (mmol g ⁻¹)			
I	Co ₁₀ /Beta(25)	Co ₃ O ₄	164	0.24	237	0.43	371	0.66	1.33	0.17	1.16	0.15	
II	Co ₁₀ Mo ₅ /Beta(25)	Co ₃ O ₄ + CoMoO ₄ + MoO ₃	167	0.30	247	0.54	396	0.53	1.37	0.19	1.18	0.16	
	Co ₁₀ Mo ₁₀ /Beta(25)		164	0.26	240	0.47	386	0.47	1.20	0.18	1.02	0.18	
III	Co ₅ Mo ₁₀ /Beta(25)		164	0.37	242	0.53	393	0.47	1.37	0.20	1.17	0.17	
	Co ₃ Mo ₁₀ /Beta(25)	CoMoO ₄ + MoO ₃	164	0.30	231	0.53	416	0.31	1.14	0.21	0.93	0.23	
IV	Co ₂ Mo ₁₀ /Beta(25)		163	0.32	238	0.59	426	0.29	1.20	0.31	0.89	0.35	
	Mo ₁₀ /Beta(25)	MoO ₃	167	0.31	258	0.66	395	0.23	1.19	0.78	0.41	1.89	
	Beta(25)	—	171	0.35	276	0.79	453	0.11	1.24	0.58	0.66	0.88	

^a Peak temperature and the corresponding amounts of acid sites calculated from the deconvolution results of NH₃-TPD profiles (Fig. S3). ^b Quantity of Brønsted (B) and Lewis (L) acid sites determined by multiplying the B/L ratio from FTIR spectra of adsorbed pyridine and the total acid sites concentration from NH₃-TPD profiles.

Table 2 Catalytic activity of methyl palmitate over the Co- or/and Mo-supported Beta(25) zeolites catalysts

Catalyst	Gas product		Organic liquid product										Yield of jet fuel range hydrocarbons (C ₈ -C ₁₆ , %)	Isomer ratio in C ₈ -C ₁₆ (%)
	Conv. (%)	Yield (%)	Selectivity (wt%)											
			C ₅ -C ₇	C ₈ -C ₁₆	C ₁₇ -C ₁₈	C ₃₂ H ₆₄ O ₂	Palmitic acid	Yield of jet fuel range hydrocarbons (C ₈ -C ₁₆ , %)	$\frac{n-C_{16}}{n-C_{15} + n-C_{16}}$					
Beta(25)	40.1	7.9	0	0	0	0	0	0	0	100	0	—	—	
Co ₁₀ /Beta(25)	100	26.1	20.2	79.1	0	0	0	0	0	0	56.5	0.69	74.9	
Co ₁₀ Mo ₅ /Beta(25)	99.9	24.2	14.3	84.1	1.5	0	0	0	0.1	0	64.7	0.66	82.0	
Co ₁₀ Mo ₁₀ /Beta(25)	99.9	23.0	13.2	85.1	1.6	0.1	0	0	0	0	65.5	0.68	82.3	
Co ₅ Mo ₁₀ /Beta(25)	94.2	10.4	6.3	89.7	2.4	1.6	0	0	0	0	80.4	0.65	83.8	
Co ₃ Mo ₁₀ /Beta(25)	61.0	11.1	88.9	0	15.6	0	41.4	43.1	13.9	77.0	14.4	0.65	72.3	
Co ₂ Mo ₁₀ /Beta(25)	37.8	6.2	93.8	0	15.3	0	7.7	77.0	14.4	95.5	0	1.00	78.2	
Mo ₁₀ /Beta(25)	25.2	4.9	95.1	0	0	0	4.5	95.5	0	0	0	—	—	

3.3 Catalytic property in one-step hydrotreatment of methyl palmitate

The catalytic performance of the Co- or/and Mo-supported Beta(25) zeolites was evaluated in one-step hydrotreatment of methyl palmitate in a semi-batch reactor at 280 °C and 20 bar of H₂ pressure during 120 min and their catalytic activities are shown in Table 2. When it comes to hydrotreatment of methyl palmitate over zeolite catalysts, the acid sites of zeolites are responsible for isomerization and cracking by the generation of carbenium ions,⁵⁰ so it can be deactivated by coke formation at high temperature during the reaction despite high conversion at initial stage.¹⁷ Because of this, the corresponding catalytic reaction condition was chosen to stably monitor the catalytic properties of the prepared catalysts based on the previous related literature performed in the temperature range of 260–300 °C.^{1,9,17,51} In Scheme 1, the simplified reaction pathway in one-step hydrotreatment of methyl palmitate was based on the earlier proposed reaction pathways and the obtained results. C₁₆ alkanes can be obtained through (i) hydrodeoxygenation without carbon loss in long alkyl chain of methyl palmitate, and C₁₅ alkanes can be produced through (ii) decarbonylation or decarboxylation with removal of carboxyl group by releasing carbon monoxide with water or carbon dioxide, respectively. Then, consecutive catalytic reactions, such as hydrogenation, dehydrogenation, cracking, and isomerization result in the formation of alkanes with carbon numbers lower than 15. In addition, palmitic acid and C₃₂H₆₄O₂ are detected as primary intermediate before the above catalytic reactions and esterification of palmitic acid, respectively^{7,10} proceed. In this regard, the liquid products were classified as alkanes with the carbon numbers of 5–7 (C₅–C₇), 8–16 (C₈–C₁₆), 17–18 (C₁₇–C₁₈), and C₃₂H₆₄O₂, and palmitic acid. The gas products included alkanes with low carbon numbers less than 4, dimethyl ether, CO, and CO₂. In the production of jet fuel, it is meaningful to focus on the yield of jet fuel range hydrocarbons in C₈–C₁₆ range alkanes.

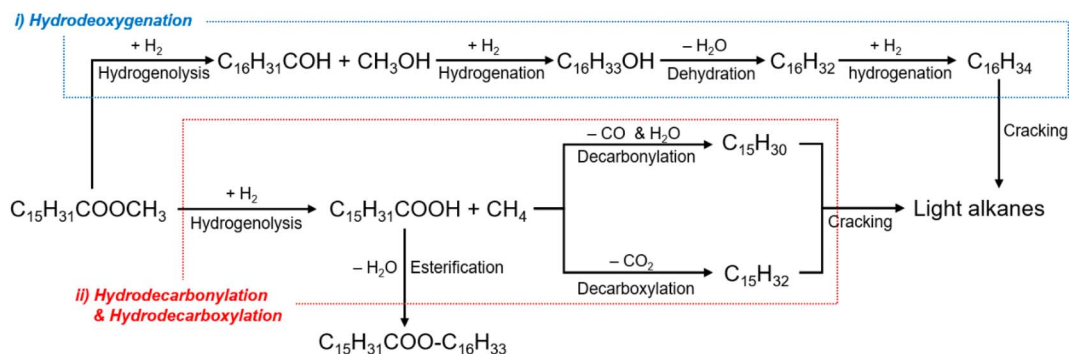
As shown in Table 2, Beta(25) zeolite used as support showed a low conversion of 40.1% and palmitic acid selectivity of 100 wt% as a major product in the organic liquid product. It is already known that the transformation of methyl palmitate to palmitic acid is catalyzed by L acid sites.⁸ Although palmitic acid is straightforwardly formed by L acid sites on Beta(25) zeolites, alkanes with carbon numbers lower than 15 were not

observed. It can be deduced that Beta(25) zeolite cannot lead to the next reaction pathways such as deoxygenation, decarboxylation, or decarbonylation, so none of the expected hydrocarbon products were observed.^{8,14}

In the case of the Mo₁₀/Beta(25) catalyst after wet impregnation of Mo, a lower conversion of 25.2% compared to Beta(25) zeolite was obtained. Similar to the product distribution of Beta(25) zeolites, the Mo₁₀/Beta(25) catalyst showed selectivity toward palmitic acid (95.5 wt%) as a major liquid product and C₃₂H₆₄O₂ (4.5 wt%) as a minor liquid product. With low acid site concentration on the Mo₁₀/Beta(25), the weak acid sites involved by Mo species seem to be insufficient to facilitate catalytic reactions except hydrogenolysis of methyl palmitate.

To confirm that the bottleneck of further catalytic reaction for jet fuel range hydrocarbon over the Beta(25) and Mo₁₀/Beta(25) catalysts is DO, the catalytic conversion of palmitic acid (PA) and hexadecane (HD) were investigated, as shown in Table 3. For the production of light alkanes, PA should be subjected to DO through decarbonylation or decarboxylation like methyl palmitate, but HD is enough through cracking. In the case of PA, the conversions over the Beta(25) and Mo₁₀/Beta(25) catalysts were very low, 9.5% and 3.9%, respectively, and light alkanes from cracking were not detected. However, HD was completely decomposed to light alkanes with 100% conversion, so the gas product yield also increased to 42.7% and 35.5% over Beta(25) and Mo₁₀/Beta(25), respectively. This proves the possibility of the cracking and isomerization steps with the Beta(25) and Mo₁₀/Beta(25) catalysts, unlike DO. Moreover, wet-impregnated Mo can be used to suppress the degree of cracking according to the decreased yield of cracked light alkanes in comparison between the Beta(25) and Mo₁₀/Beta(25) catalysts, which is consistently observed during the conversion of methyl palmitate.

Over the Co₁₀/Beta(25) catalyst, the conversion was significantly raised to 100%, and alkanes with carbon numbers lower than 15 were observed as a result of the subsequent catalytic conversion, as shown in Table 2. Thus, the yield of jet fuel range hydrocarbons reached 56.5%. It is noteworthy that *n*-C₁₆ and *n*-C₁₅ alkanes were simultaneously detected with the *n*-C₁₆/*n*-C₁₅ + *n*-C₁₆ ratio of 0.69. This result indicates that methyl palmitate over the Co₁₀/Beta(25) catalyst converted along with the competing reaction pathways between hydroxylation for *n*-



Scheme 1 Simplified reaction pathway for catalytic hydrotreatment of methyl palmitate.

Table 3 Catalytic activity of PA (palmitic acid) and HD (hexadecane) over Beta(25) and Mo₁₀/Beta(25) zeolite catalysts

Reactant	Catalyst	Conv. (%)	Gas product		Organic liquid product							Yield of jet fuel range hydrocarbons (C ₈ –C ₁₆ , %)	$\frac{n\text{-C}_{16}/(n\text{-C}_{15} + n\text{-C}_{16})}{n\text{-C}_{16}}$	Isomer ratio in C ₈ –C ₁₆ (%)
			Yield (%)	Yield (%)	C ₅ –C ₇	C ₈ –C ₁₆	C ₁₇ –C ₁₈	C ₃₂ H ₆₄ O ₂	Palmitic acid	Selectivity (wt%)				
										Yield (%)	Yield (%)			
PA	Beta(25)	9.5	7.0	93.0	0	0	22.2	77.8	0	0	0	—	—	
	Mo ₁₀ /Beta(25)	3.9	3.9	96.1	0	0	43.5	56.5	0	0	0	—	—	
HD	Beta(25)	100	42.7	57.3	41.9	58.1	0	0	0	0	33.3	0.80	78.1	
	Mo ₁₀ /Beta(25)	100	35.5	64.5	31.0	69.0	0	0	0	0	44.5	0.93	63.7	

C₁₆ and decarboxylation/decarbonylation for *n*-C₁₅. Therefore, the wet-impregnated Co active for decarbonylation or decarboxylation should be contained for converting methyl palmitate into jet fuel range hydrocarbons (C₈–C₁₆). According to the NH₃-TPD and FT-IR spectra after pyridine desorption, as shown in Table 1, the introduction of a Co catalyst enables the generation of strong L acid sites, which contribute to the catalysis of not only decarboxylation/decarbonylation but also hydrodeoxygenation with weak L acid sites on the surface of Beta(25) zeolites.¹⁴ Then, the *n*-alkanes generated from the above reaction pathways would be isomerized on the metal sites and the B acid sites of Beta(25) zeolites, thus exhibiting an isomer ratio of 74.9% in the range of C₈–C₁₆.^{10,14} The isomer ratio can reflect the quality of the product as bio jet fuel because the isomerization converts the unsaturated compounds into the branched compounds, which are favorable for combustion quality with high octane number.

As for raising the yield of alkanes in the range of C₈–C₁₆ as desirable products for jet fuel range hydrocarbons, Co₁₀/Beta(25) is required to reduce unnecessary cracking including a high gas yield of 26.1% and C₅–C₇ selectivity of 20.2 wt% in the organic liquid product. In this respect, the Co-supported Beta(25) catalyst was modified by adding Mo, and catalytic testing of samples was conducted to find the optimized composition of Co and Mo for high selectivity of C₈–C₁₆ (Fig. 6). In one approach, the loading amount of Mo was increased from Co₁₀Mo₅/Beta(25) to Co₁₀Mo₁₀/Beta(25) on the basis of Co₁₀/Beta(25) as shown in Fig. 6a (see also Table 2). Our findings confirmed the deactivation of cracking by Mo in Mo₁₀/Beta(25), and the addition of Mo to Co₁₀/Beta(25) improved the C₈–C₁₆ selectivity of 85.1 wt% by decreasing the gas yield and C₅–C₇ selectivity to 23.0% and 13.2 wt%, respectively. However, there is a limitation to further raising the yield for desirable C₈–C₁₆ by increasing the Mo loading; the similar product distributions were observed for Co₁₀Mo₅/Beta(25) and Co₁₀Mo₁₀/Beta(25) as 64.7% and 65.5%, respectively. In another approach, the loading amount of Co was increased from Mo₁₀/Beta(25) to Co₁₀Mo₁₀/Beta(25) on the basis of Mo₁₀/Beta(25) as shown in Fig. 6b (see also Table 2). By increasing the amount of added Co, the conversion was improved, and the product distribution shifted to light alkanes. Until Co₂Mo₁₀/Beta(25) and Co₃Mo₁₀/Beta(25), the increased Co content resulted in the dominant esterification of palmitic acid to C₃₂H₆₄O₂. Then, the significant improvement was achieved with Co₅Mo₁₀/Beta(25); it exhibited the conversion of 94.2% and the C₈–C₁₆ selectivity of 89.7 wt% without palmitic acid remaining in the liquid product. The conversion was consistently improved over Co₁₀Mo₁₀/Beta(25) with 99.9%. These dramatic catalytic improvements from the Co₅Mo₁₀/Beta(25) catalyst seem to originate from the different acidic property with the rapidly increase in the quantity of strong L acid sites, which can catalyze not only decarboxylation/decarbonylation but also hydrodeoxygenation as explained above for Co₁₀/Beta(25). However, the higher Co loading amount in Co₁₀Mo₁₀/Beta(25) led to reduced C₈–C₁₆ selectivity due to excessive cracking. Thus, Co₅Mo₁₀/Beta(25) exhibited the best catalytic activity achieving the yield of fuel range hydrocarbons of 80.4% as desirable products for bio jet fuel

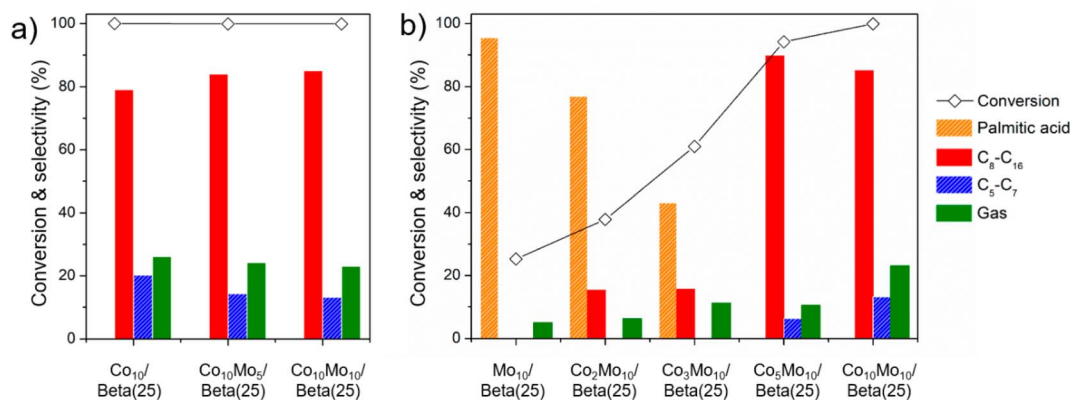


Fig. 6 Catalytic activities of methyl palmitate according to the effect of (a) the increased Mo content in the Co₁₀/Beta(25) and (b) the increased Co content in the Mo₁₀/Beta(25).

production. In addition, the isomer ratio in C₈-C₁₆ showed a similar tendency to the C₈-C₁₆ selectivity, so Co₅Mo₁₀/Beta(25) obtained the highest isomer ratio in C₈-C₁₆ as 83.8%. It is also remarkably improved catalytic activity than those of the previous catalysts performed for targeting bio jet fuel range hydrocarbons from FAMES as shown in Table S2,[†] such as Ni/desilicated meso Y zeolite (the C₈-C₁₆ selectivity of 64.8%, the isomer ratio in C₈-C₁₆ of 19.4%).¹⁸

However, there is still doubt about the requirement of bimetal co-introduced onto the support, so the Co₁₅/Beta(25) catalyst was compared with the same metal loading amount with Co₅Mo₁₀/Beta(25). Except the fact that the wet-impregnated Co of Co₁₅/Beta(25) had Co₃O₄ crystalline phase (Fig. S5[†]), the quantity of total acid sites and the distribution of B and L acid sites in Co₁₅/Beta(25) were similar to those in Co₅Mo₁₀/Beta(25) (Table S3 and Fig. S6[†]). In addition, as discussed about the strong L acid site formation by Co₃O₄, the IR peak of 1550 cm⁻¹ representing Brønsted acid sites was hardly detected in Co₁₅/Beta(25) and it can be seen that all acid sites exhibit the characteristics of Lewis acid sites (Fig. S6b[†]). Over Co₁₅/Beta(25), as seen in Table S4,[†] the high C₈-C₁₆ selectivity of 89.6 wt% was achieved, which is comparable to that of Co₅Mo₁₀/Beta(25), but the gas product yield increased by 2.6 times and resulted in lowering the C₈-C₁₆ yield to 65.1%. The isomerization also did not proceed well under the promoted cracking, resulting in 77.7% of the isomer ratio in C₈-C₁₆. This proves the necessity of co-impregnation of Co and Mo to suppress unnecessary cracking steps and overcome the limitation of single metal-supported zeolites due to not only the metal itself but also the effect of bimetal co-introduced onto the support.

Based on the above findings from hydrotreatment of methyl palmitate over the Co- and Mo-supported Beta(25) zeolites, deoxygenation of methyl palmitate is preceded by Co with the aid of strong L acid sites. In the absence of Co, palmitic acid and C₃₂H₆₄O₂ are only obtained, which can be achieved before deoxygenation, as in Mo₁₀/Beta(25) and Beta(25). Then, C₁₆ alkanes and C₁₅ alkanes are simultaneously obtained through not only decarboxylation/decarbonylation but also

hydrodeoxygenation, and the subsequent cracking and isomerization result in alkanes with carbon numbers lower than 15 and isomerized hydrocarbons. The introduction of Mo can suppress the cracking and increase the selectivity for light alkanes, and Beta(25) can enhance isomerization with hydrogenation promoted by Co. For better selectivity to jet fuel range hydrocarbons, co-impregnation of Co and Mo is necessary to overcome the limitation of single metal-supported zeolites, which can exploit the catalytic property of metal itself as well as the optimized acidic property according to the Co/Mo ratio with the appearance of CoMoO₄ as weak L acid.

4. Conclusion

The Co- or/and Mo-supported Beta(25) zeolites were investigated with different Co/Mo composition ratio for hydrotreatment of methyl palmitate. The variation of the Co/Mo composition ratio led to a distinct change in the metal phase due to the preference for the formation of CoMoO₄ than mono metal oxides. Furthermore, the acidic property was strongly dependent on the Co metal phase altered by the Co/Mo ratio because L acid sites with different strength were formed such as Co₃O₄ for strong L acid sites and CoMoO₄ for weak L acid sites. In hydrotreatment of methyl palmitate with the Co- or Mo-supported Beta(25) zeolite as monometallic catalyst, impregnated Co was found to be essential for decarbonylation/decarboxylation to convert methyl palmitate into jet fuel range hydrocarbons (C₈-C₁₆), and impregnated Mo was used to suppress the degree of cracking. As bimetallic catalyst, the Co and Mo-supported Beta(25) zeolite was beneficial to improve the C₈-C₁₆ selectivity by optimizing the acidic properties to inhibit excessive cracking. Co₅Mo₁₀/Beta(25) zeolites achieved the highest C₈-C₁₆ selectivity of 89.7 wt% including isomer ratio of 83.8% in organic liquid product with the conversion of 94.2%. This work provides a meaningful reference for Co- and Mo-supported Beta zeolite as transition metal-supported zeolite catalysts with unique modifications of acidic properties and optimal catalytic properties for selective one-step hydrotreatment to produce bio jet fuel range hydrocarbons.

Conflicts of interest

There are no conflicts to declare.

Acknowledgements

This work was supported by the Korea Institute of Energy Technology Evaluation and Planning (KETEP) and the Ministry of Trade, Industry & Energy (MOTIE) of the Republic of Korea (No. 20212010200100).

References

- 1 Y. Shi, Y. Cao, Y. Duan, H. Chen, Y. Chen, M. Yang and Y. Wu, *Green Chem.*, 2016, **18**, 4633–4648.
- 2 G. W. Huber, S. Iborra and A. Corma, *Chem. Rev.*, 2006, **106**, 4044–4098.
- 3 Y. Du, F. Wang, X. Xia, H. Zhu, Z. Zhang, C. You, X. Jiang, J. Jiang and C. Li, *Renewable Energy*, 2022, **198**, 246–253.
- 4 C. Zhang, X. Hui, Y. Lin and C.-J. Sung, *Renewable Sustainable Energy Rev.*, 2016, **54**, 120–138.
- 5 F. P. Sousa, L. N. Silva, D. B. de Rezende, L. C. A. de Oliveira and V. M. D. Pasa, *Fuel*, 2018, **223**, 149–156.
- 6 E. S. K. Why, H. C. Ong, H. V. Lee, Y. Y. Gan, W.-H. Chen and C. T. Chong, *Energy Convers. Manage.*, 2019, **199**, 112015.
- 7 Y. Bie, J. Lehtonen and J. Kanervo, *Appl. Catal., A*, 2016, **526**, 183–190.
- 8 I. V. Deliy, E. N. Vlasova, A. L. Nuzhdin, E. Y. Gerasimov and G. A. Bukhtiyarova, *RSC Adv.*, 2014, **4**, 2242–2250.
- 9 B. Ma and C. Zhao, *Green Chem.*, 2015, **17**, 1692–1701.
- 10 L. Chen, J. Fu, L. Yang, Z. Chen, Z. Yuan and P. Lv, *ChemCatChem*, 2014, **6**, 3482–3492.
- 11 E. W. Ping, R. Wallace, J. Pierson, T. F. Fuller and C. W. Jones, *Microporous Mesoporous Mater.*, 2010, **132**, 174–180.
- 12 Z. Zhang, F. Wang, J. Jiang, H. Zhu, Y. Du, J. Feng, H. Li and X. Jiang, *Fuel*, 2023, **333**, 126341.
- 13 H. Zhu, F. Wang, J. Jiang, Z. Zhang, Y. Du, J. Feng and X. Jiang, *Fuel Process. Technol.*, 2023, **239**, 107537.
- 14 C. Wang, Z. Tian, L. Wang, R. Xu, Q. Liu, W. Qu, H. Ma and B. Wang, *ChemSusChem*, 2012, **5**, 1974–1983.
- 15 S. Kovács, T. Kasza, A. Thernesz, I. W. Horváth and J. Hancsók, *Chem. Eng. J.*, 2011, **176–177**, 237–243.
- 16 V. A. Yakovlev, S. A. Khromova, O. V. Sherstyuk, V. O. Dundich, D. Y. Ermakov, V. M. Novopashina, M. Y. Lebedev, O. Bulavchenko and V. N. Parmon, *Catal. Today*, 2009, **144**, 362–366.
- 17 H. Imai, M. Abe, K. Terasaka, H. Yamazaki, R. Osuga, J. N. Kondo and T. Yokoi, *Fuel Process. Technol.*, 2020, **197**, 106182.
- 18 Z. Zhang, J. Cheng, Y. Qiu, X. Zhang, J. Zhou and K. Cen, *Fuel*, 2019, **244**, 472–478.
- 19 J. Y. Jeon, Y. Han, Y.-W. Kim, Y.-W. Lee, S. Hong and I. T. Hwang, *Biofuels, Bioprod. Biorefin.*, 2019, **13**, 690–722.
- 20 P. Chintakanan, T. Vitidsant, P. Reubroycharoen, P. Kuchonthara, T. Kida and N. Hinchiranan, *Fuel*, 2021, **293**, 120472.
- 21 I.-H. Choi, K.-R. Hwang, J.-S. Han, K.-H. Lee, J. S. Yun and J.-S. Lee, *Fuel*, 2015, **158**, 98–104.
- 22 J. E. Herrera, L. Balzano, A. Borgna, W. E. Alvarez and D. E. Resasco, *J. Catal.*, 2001, **204**, 129–145.
- 23 Y. Chen, Z. Tian, Q. Liu and B. Bian, *Sustainable Energy Fuels*, 2020, **4**, 3042–3050.
- 24 K. Shimura, T. Miyazawa, T. Hanaoka and S. Hirata, *Appl. Catal., A*, 2015, **494**, 1–11.
- 25 J. Janas, T. Machej, J. Gurgul, R. P. Socha, M. Che and S. Dzwigaj, *Appl. Catal., B*, 2007, **75**, 239–248.
- 26 B. de Rivas, R. López-Fonseca, C. Jiménez-González and J. I. Gutiérrez-Ortiz, *J. Catal.*, 2011, **281**, 88–97.
- 27 Q. Yu, L. Zhang, R. Guo, J. Sun, W. Fu, T. Tang and T. Tang, *Fuel Process. Technol.*, 2017, **159**, 76–87.
- 28 L. Zhang, Q. Dai, W. Fu, T. Tang, P. Dong, M. He and Q. Chen, *J. Catal.*, 2018, **359**, 130–142.
- 29 P. A. Nikulshin, D. I. Ishutenko, A. A. Mozhaev, K. I. Maslakov and A. A. Pimerzin, *J. Catal.*, 2014, **312**, 152–169.
- 30 E. Payen, J. Grimblot and S. Kasztelan, *J. Phys. Chem.*, 1987, **91**, 6642–6648.
- 31 W. Fu, L. Zhang, D. Wu, M. Xiang, Q. Zhuo, K. Huang, Z. Tao and T. Tang, *J. Catal.*, 2015, **330**, 423–433.
- 32 W. Li, G. D. Meitzner, R. W. Borry and E. Iglesia, *J. Catal.*, 2000, **191**, 373–383.
- 33 K. Chen, S. Xie, A. T. Bell and E. Iglesia, *J. Catal.*, 2001, **198**, 232–242.
- 34 F. Nti, D. A. Anang and J. I. Han, *J. Alloys Compd.*, 2018, **742**, 342–350.
- 35 G. Zhang, D. Wang, P. Feng, S. Shi, C. Wang, A. Zheng, G. Lü and Z. Tian, *Chin. J. Catal.*, 2017, **38**, 1207–1215.
- 36 X. Li, W. Zhang, X. Li, S. Liu, H. Huang, X. Han, L. Xu and X. Bao, *J. Phys. Chem. C*, 2009, **113**, 8228–8233.
- 37 A. Y. Stakheev and W. M. H. Sachtler, *J. Chem. Soc., Faraday Trans.*, 1991, **87**, 3703–3708.
- 38 T. M. Tri, J. P. Candy, P. Gallezot, J. Massardier, M. Prlmet, J. C. Védrine and B. Imelik, *J. Catal.*, 1983, **79**, 396–409.
- 39 Y. Liu, Y. Xing, S. Xu, Y. Lu, S. Sun and D. Jiang, *Chem. Eng. J.*, 2022, **431**, 133240.
- 40 D. P. Upare, S. Park, M. S. Kim, J. Kim, D. Lee, J. Lee, H. Chang, W. Choi, S. Choi, Y. P. Jeon, Y. K. Park and C. W. Lee, *J. Ind. Eng. Chem.*, 2016, **35**, 99–107.
- 41 M. de Boer, E. P. F. M. Koch, R. J. Blaauw, E. R. Stobbe, A. N. J. M. Hoffman, L. A. Boot, A. J. van Dillen and J. W. Geus, *Solid State Ionics*, 1993, **63–65**, 736–742.
- 42 J. Chen, Y. Ge, Q. Feng, P. Zhuang, H. Chu, Y. Cao, W. R. Smith, P. Dong, M. Ye and J. Shen, *ACS Appl. Mater. Interfaces*, 2019, **11**, 9002–9010.
- 43 M. H. M. Ahmed, O. Muraza, A. K. Jamil, E. N. Shafei, Z. H. Yamani and K.-H. Choi, *Energy Fuels*, 2017, **31**, 5482–5490.
- 44 Q. Liu, Y. Bie, S. Qiu, Q. Zhang, J. Sainio, T. Wang, L. Ma and J. Lehtonen, *Appl. Catal., B*, 2014, **147**, 236–245.
- 45 M. Rutkowska, Z. Piwowarska, E. Micek and L. Chmielarz, *Microporous Mesoporous Mater.*, 2015, **209**, 54–65.

- 46 D. Kubička, N. Kumar, T. Venäläinen, H. Karhu, I. Kubičková, H. Österholm and D. Y. Murzin, *J. Phys. Chem. B*, 2006, **110**, 4937–4946.
- 47 T. M. Salama, I. Othman, M. Sirag and G. A. El-Shobaky, *Microporous Mesoporous Mater.*, 2006, **95**, 312–320.
- 48 S. Rajagopal, J. A. Marzari and R. Miranda, *J. Catal.*, 1995, **151**, 192–203.
- 49 F. E. Kiviat and L. Petrakis, *J. Phys. Chem.*, 1973, **77**, 1232–1239.
- 50 W. Luo, W. Cao, P. C. A. Bruijninx, L. Lin, A. Wang and T. Zhang, *Green Chem.*, 2019, **21**, 3744–3768.
- 51 B. Peng, Y. Yao, C. Zhao and J. A. Lercher, *Angew. Chem., Int. Ed.*, 2012, **51**, 2072–2075.